Journal of Applied Physics ARTICLE pubs.aip.org/aip/jap

Accelerated phonon transport calculations for nanostructures: Combining neuroevolution potentials and compressed sensing

Cite as: J. Appl. Phys. **139**, 135103 (2026); doi: 10.1063/5.0324012
Submitted: 21 January 2026 · Accepted: 16 March 2026 ·
Published Online: 1 April 2026

Fei Yin,[1] Shixian Liu,[1,a)] Yiming Dong,[1] A. A. Barinov,[1] Ke Xu,[2,b)] and V. I. Khvesyuk[1,c)]

AFFILIATIONS

[1]Department of Thermophysics, Bauman Moscow State Technical University, Moscow 105005, Russia
[2]College of Physical Science and Technology, Bohai University, Jinzhou, China

[a)]**Author to whom correspondence should be addressed:** sxliu98@gmail.com
[b)]**Email:** kickhsu@gmail.com
[c)]**Email:** khvesyuk@bmstu.ru

ABSTRACT

Thermal management in nanostructured devices necessitates the accurate and efficient prediction of phonon transport properties. However, solving the Boltzmann transport equation via first-principles calculations is often computationally prohibitive due to the extensive supercells required to model realistic nanostructures. In this work, we present an accelerated, automated workflow that synergizes neuroevolution potentials with compressed sensing techniques to efficiently extract high-order anharmonic force constants. We validate this approach using silicon thin films as a prototype, explicitly accounting for the complexities of surface reconstruction. Our results demonstrate that this framework achieves accuracy comparable to density functional theory while reducing the computational cost by several orders of magnitude. The workflow successfully reproduces phonon dispersion relations and captures the temperature- and size-dependent trends of lattice thermal conductivity, incorporating the critical contribution of inter-mode coherence. This methodology offers a scalable and robust solution for the high-throughput thermal characterization of low-dimensional materials.

I. INTRODUCTION

In the post-Moore era, as micro- and nanoelectronic devices approach atomic limits, thermal dissipation has become a critical bottleneck limiting the performance and stability of high-power chips.[1,2] Unlike bulk materials, thermal transport in nanostructures is governed by strong phonon boundary scattering[3–7] and spatial confinement effects,[8–12] resulting in intrinsically size-dependent properties. Accurate prediction of lattice thermal conductivity (κ) in this regime is, therefore, essential, not only for elucidating microscopic transport mechanisms but also for guiding the thermal design of next-generation devices.

The first-principles phonon Boltzmann transport equation (BTE) constitutes the standard framework for such calculations.[13–18] Although the iterative solution of the BTE is required for full accuracy, the relaxation time approximation (RTA) provides a reliable description for systems dominated by resistive Umklapp (U) scattering. While the BTE treats anharmonic scattering rigorously, its application is severely constrained by the computational cost of extracting high-order interatomic force constants (IFCs).[15] Standard finite-displacement methods (FDMs) based on density functional theory (DFT) scale steeply with system size [typically $O(N^3)$ to $O(N^4)$].[15,16,19] This scaling creates a prohibitive barrier for low-dimensional nanostructures, where supercells containing hundreds of atoms are necessitated to capture surface reconstructions and decouple periodic images. At this scale, direct DFT approaches become computationally intractable.

Machine learning potentials (MLPs) provide a robust pathway to circumvent this efficiency-accuracy trade-off.[20–29] By constructing the potential energy surface (PES) from DFT training data, MLPs enable simulations of large-scale systems with *ab initio* accuracy at a fraction of the cost. Among these, Neuroevolution Potentials (NEP)[30–32] are particularly notable for their exceptional computational throughput and transferability.[33–35] Their capacity to model complex many-body interactions allows them to surpass

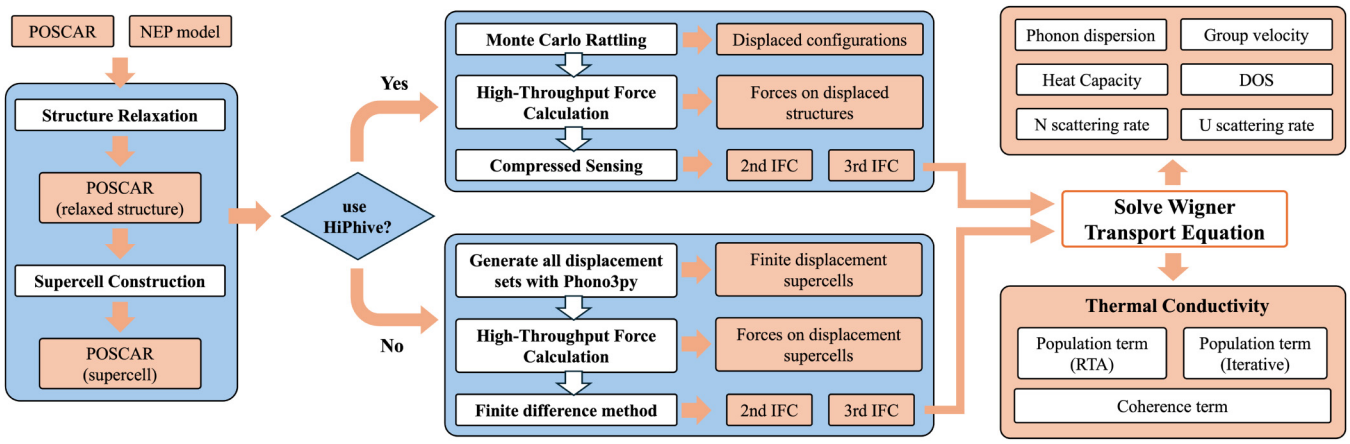

FIG. 1. Schematic of the accelerated computational workflow for phonon transport calculations. Starting from the input POSCAR (the crystal structure input file used in VASP) and NEP model, the structure is relaxed and expanded into a supercell. Displaced configurations are then generated either via Monte Carlo rattling (for HiPhive) or via finite displacements (for Phono3py). The resulting forces and configurations are used to extract second- and third-order interatomic force constants (IFCs). These IFCs serve as inputs to the Wigner transport equation (WTE) solver, yielding phonon dispersion, group velocities, scattering rates, and the decomposed lattice thermal conductivity κ_p and κ_c.

standard empirical force fields, making them ideally suited for describing the anharmonic features inherent to nanostructures.[36–39]

Complementary to efficient PES exploration, compressed sensing (CS) offers a rigorous method for handling the combinatorial complexity of force constant extraction. Unlike FDM, which necessitates exhaustive sampling of the configuration space, CS-based tools like HiPhive[40,41] exploit the physical sparsity of the interaction space. By recovering force constants from a minimal set of reference configurations, CS renders the extraction process feasible even in data-scarce regimes.

Despite these advances, applying these techniques to realistic nanostructures presents unique challenges. Systems undergoing surface reconstruction involve symmetry breaking and increased degrees of freedom,[42] which hinder efficient sampling of the PES. For such low-symmetry systems, a unified workflow that tightly couples high-fidelity MLP sampling with sparse parameter extraction is imperative to rigorously predict thermal properties.

The transport formalism itself also requires an update. Standard BTE relies on a particle picture that misses inter-band coherence effects. In nanostructures, however, surface reconstruction leads to extensive band folding and mode mixing, making these wave-like contributions significant.[5] The Wigner transport equation (WTE) is, thus, essential to rigorously treat both particle and wave nature of heat transport.[43,44]

In this work, we present an integrated computational framework coupling NEP with CS to accelerate the prediction of phonon transport properties. We validate this methodology on silicon thin films, explicitly accounting for surface reconstruction effects. Our results demonstrate that this approach reproduces DFT-level phonon dispersion and lattice thermal conductivity calculated via the WTE formalism, all while reducing computational costs by several orders of magnitude. This framework provides a practical and scalable route for the high-throughput thermal characterization of complex, low-dimensional materials.

II. METHODOLOGY

In this work, we present an automated workflow for high-fidelity predictions of lattice thermal conductivity. As illustrated in Fig. 1, our approach couples the computational efficiency of NEP with the sparse sampling capabilities of compressed sensing. The workflow consists of five key stages: (1) training the NEP model; (2) system construction and relaxation; (3) extracting second- and third-order IFCs via CS or FDM; (4) enforcing physical symmetries through rotational sum rules; and (5) solving the WTE to evaluate transport properties.

A. Neuroevolution potential model

To address the scaling limitations of direct DFT calculations, we employ the NEP framework.[30] The NEP model efficiently constructs a high-dimensional PES by mapping local atomic environments to site energies via a feed-forward neural network.

The local environment of atom i is encoded by a descriptor vector $\mathbf{q}^i = \{q_\nu^i\}_{\nu=1}^{N_{\rm des}}$, containing both radial and angular components. The site energy U_i is computed through a single hidden layer with $N_{\rm neu}$ neurons,

$$U_i = \sum_{\mu=1}^{N_{\rm neu}} w_\mu^{(2)} \tanh\left(\sum_{\nu=1}^{N_{\rm des}} w_{\mu\nu}^{(1)} q_\nu^i + b_\mu^{(1)}\right) + b^{(2)}, \quad (1)$$

where $\mathbf{w}$ and $\mathbf{b}$ denote the weight matrices and bias vectors, respectively. The model parameters are optimized by minimizing a loss function $L(\mathbf{z})$ that includes contributions from energies, forces, and virial tensors,

$$L(\mathbf{z}) = \lambda_e \Delta E_{\rm RMSE} + \lambda_f \Delta F_{\rm RMSE} + \lambda_\nu \Delta V_{\rm RMSE} + L_{\rm reg}. \quad (2)$$

Here, $L_{\rm reg}$ represents L_1 and L_2 regularization terms included to prevent overfitting. This architecture enables the NEP to describe

complex many-body interactions with *ab initio* accuracy while maintaining the computational speed required for extensive phase space sampling.

B. Force constants and compressed sensing extraction

The lattice vibrational properties are described by the Taylor expansion of the potential energy U with respect to atomic displacements $\mathbf{u}$,

$$U = U_0 + \frac{1}{2!}\sum_{ij}\Phi_{ij}^{\alpha\beta}u_i^\alpha u_j^\beta + \frac{1}{3!}\sum_{ijk}\Phi_{ijk}^{\alpha\beta\gamma}u_i^\alpha u_j^\beta u_k^\gamma + \cdots. \quad (3)$$

Here, $\Phi_{ij}^{\alpha\beta}$ and $\Phi_{ijk}^{\alpha\beta\gamma}$ denote the second-order (harmonic) and third-order (anharmonic) IFCs. Calculating these high-order terms is computationally demanding due to the combinatorial growth of degrees of freedom. Traditional over-determined approaches scale steeply ($O(N^3)$) with the supercell size.

To overcome this bottleneck, we employ CS as implemented in the HiPhive package.[40] This method exploits the intrinsic physical sparsity of the force constant vector $\mathbf{\Phi}$, specifically, the rapid decay of interaction magnitudes with interatomic distance. The extraction is formulated as a linear inverse problem $\mathbf{F} = \mathbf{M}\mathbf{\Phi}$, where $\mathbf{F}$ is the force vector computed by the NEP model and $\mathbf{M}$ is the sensing matrix derived from atomic displacements.

We solve this under-determined system using a recursive feature elimination (RFE) algorithm combined with the least absolute shrinkage and selection operator (LASSO). This iterative process isolates physically significant non-zero interaction terms while eliminating irrelevant parameters. The training set is generated via a Monte Carlo rattling method, where atoms are randomly displaced (amplitude ~ 0.01 Å for harmonic terms, larger for anharmonic) to efficiently sample the PES. This workflow allows for the robust recovery of full IFCs at a significantly reduced computational cost compared to systematic enumeration.

C. Rotational sum rules

Following the extraction of force constants, we strictly enforce rotational sum rules to ensure the physical consistency of the phonon spectrum, particularly the acoustic branches near the Γ point. We apply the Born–Huang invariance condition,

$$\sum_j \Phi_{ij}^{\alpha\beta}r_j^\gamma = \sum_j \Phi_{ij}^{\alpha\gamma}r_j^\beta, \quad (4)$$

which ensures the invariance of potential energy under rigid body rotations. Additionally, to properly describe flexural modes in low-dimensional structures, we enforce the higher-order Huang invariances,

$$\sum_{ij}\Phi_{ij}^{\alpha\beta}r_{ij}^\gamma r_{ij}^\delta = \sum_{ij}\Phi_{ij}^{\gamma\delta}r_{ij}^\alpha r_{ij}^\beta, \quad (5)$$

where r_{ij} is the relative position vector. These constraints are indispensable for obtaining accurate elastic properties and stabilizing low-frequency phonon modes.

D. Wigner phonon transport calculation

To account for both particle-like propagation and wave-like coherence effects in phonon transport, we employ the WTE formalism.[43,44] This approach generalizes the standard Boltzmann theory by decomposing the lattice thermal conductivity tensor into two contributions: a population term (κ_p) and a coherence term (κ_c),

$$\kappa^{\alpha\beta} = \kappa_p^{\alpha\beta} + \kappa_c^{\alpha\beta}. \quad (6)$$

The population term (κ_p) corresponds to the conventional transport of phonon wavepackets described by the BTE. This contribution is given by

$$\kappa_p^{\alpha\beta} = \frac{1}{Vk_BT^2}\sum_\lambda (\hbar\omega_\lambda)^2 v_\lambda^\alpha F_\lambda^\beta \bar{n}_\lambda(\bar{n}_\lambda + 1), \quad (7)$$

where $\lambda \equiv (\mathbf{q}, j)$ denotes a phonon mode with wave vector $\mathbf{q}$ and branch index j, ω_λ is the frequency, V is the system volume, and $\bar{n}_\lambda$ represents the equilibrium Bose–Einstein distribution. The vector $\mathbf{F}_\lambda$ represents the linearized deviation of the phonon distribution. Under the RTA, $\mathbf{F}_\lambda = \mathbf{v}_\lambda\tau_\lambda^{\mathrm{RTA}}$, where $\tau_\lambda^{\mathrm{RTA}}$ is the inverse of the total scattering rate. While the RTA is computationally efficient and remains accurate for systems where U scattering is dominant, a more rigorous determination of $\mathbf{F}_\lambda$ requires an iterative solution of the BTE. In such cases, $\mathbf{F}_\lambda = \mathbf{v}_\lambda\tau_\lambda^{\mathrm{eff}}$, where $\tau_\lambda^{\mathrm{eff}}$ is the effective relaxation time obtained by solving the full collision matrix.

The coherence term (κ_c) captures the heat flux arising from the tunneling between distinct phonon eigenstates. This term plays a significant role in systems with complex unit cells or significant band folding and is calculated using the off diagonal elements of the velocity operator,

$$\kappa_c^{\alpha\beta} = \frac{\hbar^2}{Vk_BT^2}\sum_{\lambda\neq\lambda'}\frac{\omega_\lambda + \omega_{\lambda'}}{2}v_{\lambda\lambda'}^\alpha v_{\lambda\lambda'}^\beta \mathcal{A}_{\lambda\lambda'}(\Gamma_\lambda + \Gamma_{\lambda'}). \quad (8)$$

Here, $v_{\lambda\lambda'}^\alpha$ represents the off diagonal velocity matrix element between modes λ and λ' in direction α. The spectral function $\mathcal{A}_{\lambda\lambda'}$, which governs the overlap of the generalized Lorentzian spectral lines of the two interacting modes, is explicitly given by

$$\mathcal{A}_{\lambda\lambda'} = \frac{\omega_\lambda\bar{n}_\lambda(\bar{n}_\lambda + 1) + \omega_{\lambda'}\bar{n}_{\lambda'}(\bar{n}_{\lambda'} + 1)}{4(\omega_{\lambda'} - \omega_\lambda)^2 + (\Gamma_\lambda + \Gamma_{\lambda'})^2}, \quad (9)$$

where Γ_λ is the phonon linewidth (i.e., the inverse phonon lifetime $\Gamma_\lambda = 1/\tau_\lambda$). Inclusion of κ_c accounts for the wave-like inter-band tunneling, which is formally absent in the BTE but becomes essential for describing thermal transport in systems with significant band mixing.

E. Computational details

To demonstrate the robustness of our automated workflow in characterizing low-dimensional thermal transport, we selected a silicon thin film as a prototype system. The atomic structure, illustrated in Fig. 2, consists of a 2 nm thick film featuring the experimentally observed 2×2 surface reconstruction.[45,46] This reconstruction is physically significant as it breaks bulk

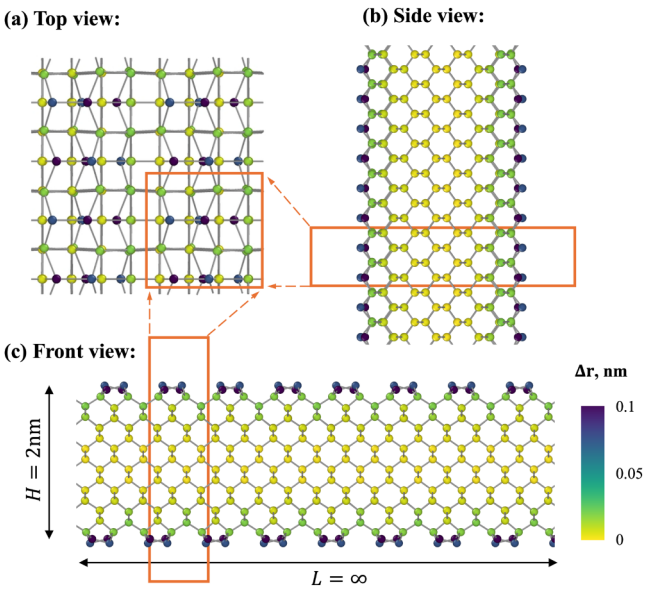

FIG. 2. Atomic structure of the 2 nm silicon thin film model viewed from the (a) top, (b) side, and (c) front perspectives. The orange dashed boxes delineate the 2 × 2 reconstructed primitive cells. The color mapping on the atoms represents the degree of reconstruction, defined as the displacement Δr relative to the ideal crystalline positions. Dark blue regions highlight the significantly distorted surface layers, while yellow regions represent the bulk-like interior. This 2 × 2 surface reconstruction introduces symmetry breaking that induces surface-localized modes, significantly modifying the phonon spectrum.

translational symmetry, inducing distinct surface-localized vibrational modes that are critical for accurately modeling phonon confinement and boundary scattering effects.

To capture the complex physics of surface reconstruction with first-principles accuracy, we employed the NEP-SiNWs potential.[37,47] This fourth-generation Neuroevolution Potential (NEP4) was optimized via the separable natural evolution strategy (SNES).[48] We ensured high transferability by training on a dataset generated through a three-stage active learning protocol: (i) an initial baseline of bulk silicon supercells; (ii) expansion to diverse nanostructures, explicitly incorporating 2 × 2 surface reconstructions; and (iii) refinement through a committee-based query strategy to fill data gaps and ensure model convergence. The final database consists of 3053 DFT reference structures, comprising 960 bulk supercells, 220 surface slabs, and 1873 nanowire configurations.

Figure 3 summarizes the training and validation performance of the NEP model. As shown in Fig. 3(a), the loss functions for energy, force, and virial terms show rapid and stable convergence. To rigorously evaluate the model's generalizability and rule out overfitting, the dataset was partitioned into a training set and a strictly held-out test set. The high fidelity of the model is further confirmed in the parity plots [Figs. 3(b)–3(d)], where predictions for both sets align closely with the identity line. The calculated root mean square errors (RMSE) on the training set are 14.42 meV/atom for energy, 143.97 meV/Å for forces, and 71.15 meV/atom for virials. While the absolute RMSE for atomic forces may appear nominally high, this is primarily a consequence of the large dynamic range of forces induced by the complex surface reconstruction. To provide a more objective assessment that facilitates cross-model comparisons, we also evaluated the relative RMSE (RRMSE)[49,50] and the coefficient of determination (R^2). Notably, the model demonstrates robust predictive capability on the unseen test set, achieving remarkably high R^2 values of 0.98 for energy, 0.91 for forces, and 0.85 for the virial tensor components. These metrics, accompanied by correspondingly low RRMSE values, confirm that the model accurately captures the underlying physical interactions rather than merely memorizing the training data. This accuracy is comparable to Gaussian Approximation Potentials (GAPs),[23] while maintaining the significantly higher computational efficiency required for the extensive sampling in this study. Detailed hyperparameters for NEP training are listed in Appendix A.

Second- and third-order IFCs were extracted via the CS formalism implemented in the HiPhive package, employing a 4 × 4 × 1 supercell. In contrast to the computationally expensive systematic enumeration typical of standard FDM, we adopted a stochastic sampling strategy. A training set of 500 randomized configurations was generated via Monte Carlo rattling with a displacement standard deviation of $\sigma = 0.03$ Å. This amplitude effectively samples the anharmonic regions of the PES while avoiding unphysical structural distortions. Interaction cutoffs were set to 5.0 Å (second-order) and 4.0 Å (third-order) to capture long-range interactions in the covalent lattice.

Lattice thermal conductivity was evaluated by solving the WTE on a 21 × 21 × 1 q-point mesh over a temperature range of 100–1000 K. The WTE formalism is critical in this context to rigorously account for both particle-like phonon populations and wave-like coherences. The latter contribution is particularly pronounced in this system due to the extensive band folding and mode mixing induced by the surface reconstruction.

The reliability of the calculation is ensured by mitigating error propagation across three stages: (i) potential level, where active learning keeps force RMSE below 0.1 eV/Å; (ii) extraction level, where N_{struc} convergence suppresses sampling uncertainty; and (iii) solution level, where q-mesh refinement ensures numerical accuracy. Detailed convergence analyses for N_{struc} and q-mesh are provided in Appendix B, while representative input scripts are included in Appendix C to assist reproducibility.

III. RESULTS AND DISCUSSION

We first assess the computational acceleration achieved by our framework. Table I benchmarks the required atomic configurations and wall-time costs against the NEP (FDM) baseline. For the bulk silicon system, the CS-NEP workflow extracts the force constants in ∼ 1.0 h using only 100 structures, achieving a 2× speedup compared to NEP (FDM) and a 10× speedup over traditional DFT. The advantage becomes absolute for the nanostructured systems. In the case of the silicon thin films, the surface reconstruction severely breaks the crystalline symmetry, yielding an exorbitant 12 956 displaced supercells for the 1 nm film, which drastically escalates to 162 568 supercells for the 2 nm film under standard FDM. This massive configuration space renders direct DFT calculations computationally intractable. While the NEP-FDM approach makes this

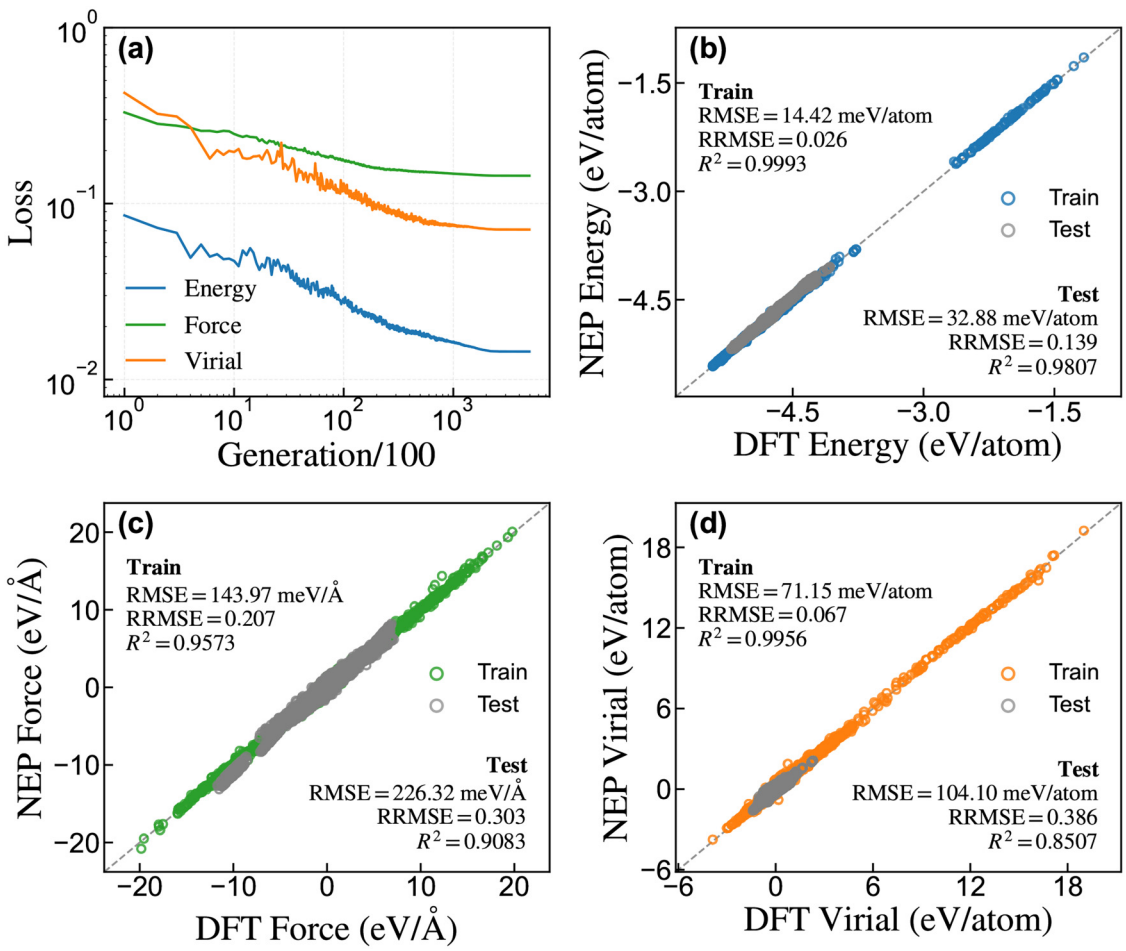

FIG. 3. Training statistics and accuracy verification of the NEP model. (a) Evolution of the loss functions for energy, force, and virial terms with respect to the number of generations, showing stable convergence. (b)–(d) Parity plots comparing the DFT-calculated and NEP-predicted values for (b) energy, (c) forces, and (d) virial. To explicitly evaluate the model's generalizability and rule out overfitting, the dataset is partitioned into a training set (colored circles) and a held-out test set (gray hollow circles). Along with the absolute root mean square error (RMSE), the relative RMSE (RRMSE) and the coefficient of determination (R^2) are annotated. The consistently high test R^2 values confirm the model's high fidelity and robust predictive capability on unseen configurations.

TABLE I. Computational cost comparison for extracting second- and third-order force constants. Costs are measured in wall-time (hours) on a single computational node. The "Speedup" factor is normalized relative to the NEP (FDM) baseline.

	Bulk silicon (2-atom primitive cell, 4 × 4 × 4 supercell)			Si thin film (1 nm) (16-atom primitive cell, 4 × 4 × 1 supercell)			Si thin film (2 nm) (32-atom primitive cell, 4 × 4 × 1 supercell)		
Method	N_{struc} [a]	Time (h)	Speedup	N_{struc}	Time (h)	Speedup	N_{struc}	Time (h)	Speedup
DFT (FDM)	542	∼10.0	0.2 ×	… [b]	…	…	…	…	…
NEP (FDM)	417	∼2.0	1 ×	12 956	∼20.0	1 ×	162 568	∼80.0	1 ×
NEP (CS)	100	∼1.0	2×	500	∼4.0	5×	500	∼10.0	8×

[a] N_{struc} denotes the number of atomic configurations used for force constant extraction with HiPhive.
[b] Computationally intractable due to the massive number of displaced supercells required by symmetry breaking from surface reconstruction.

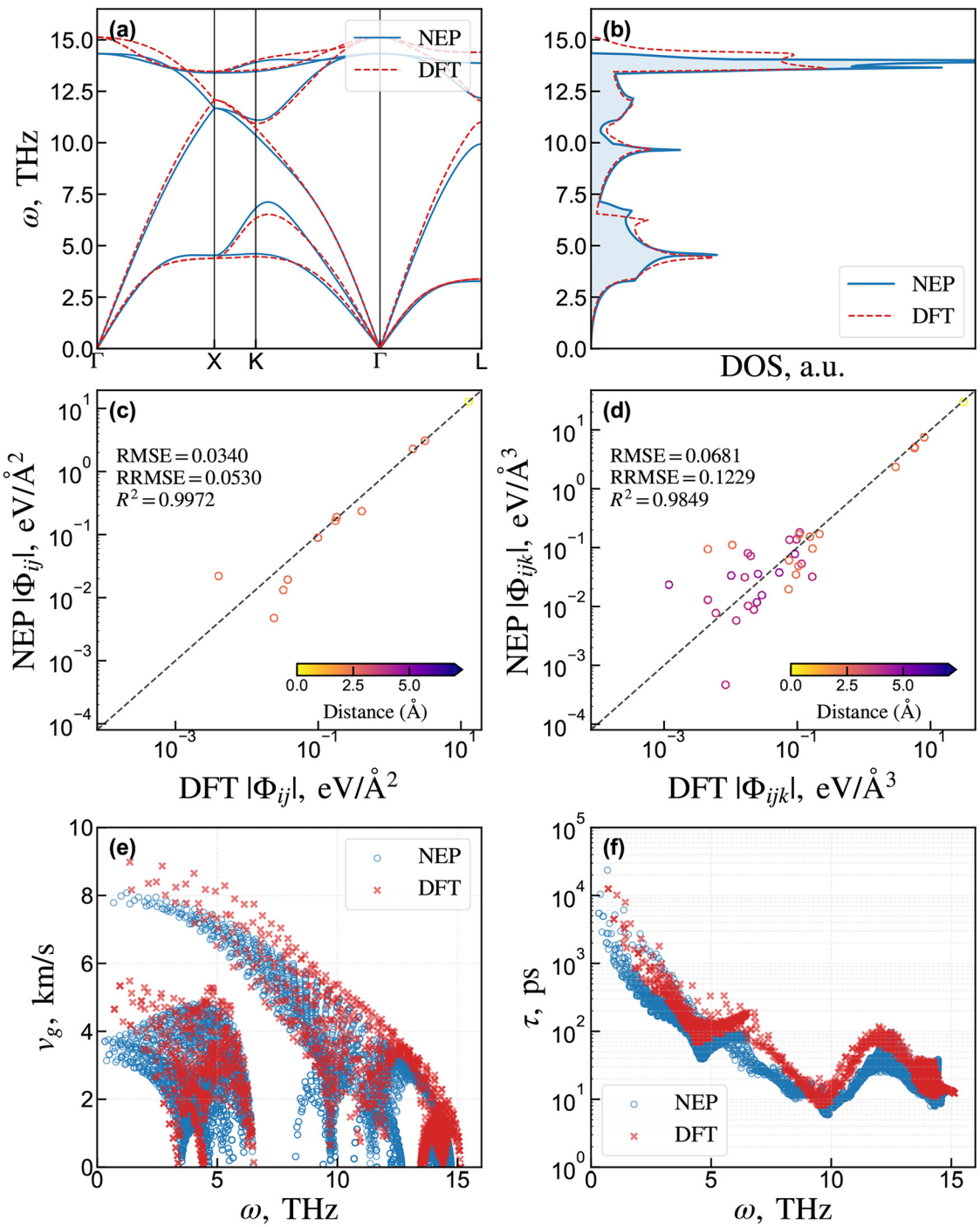

FIG. 4. Benchmarking phonon transport properties and foundational interatomic force constants (IFCs) of bulk silicon at 300 K. Comparison between the accelerated CS-NEP workflow (blue circles/lines) and standard DFT-FDM calculations (red crosses/dashed lines): (a) phonon dispersion relations along high-symmetry paths; (b) phonon density of states (DOS); (c) parity plot of the second-order IFCs (Φ_{ij}); and (d) third-order IFCs (Φ_{ijk}). The IFC plots utilize a symmetrical logarithmic scale to explicitly resolve the magnitude distributions across over four orders of magnitude, with the marker color mapped to the interatomic distance to distinguish between strong short-range and weak long-range interactions. (e) Phonon group velocities (v_g); (f) phonon relaxation times (τ) resulting from three-phonon scattering. The excellent agreement implies that the workflow accurately captures both the harmonic stiffness and anharmonic interaction strengths.

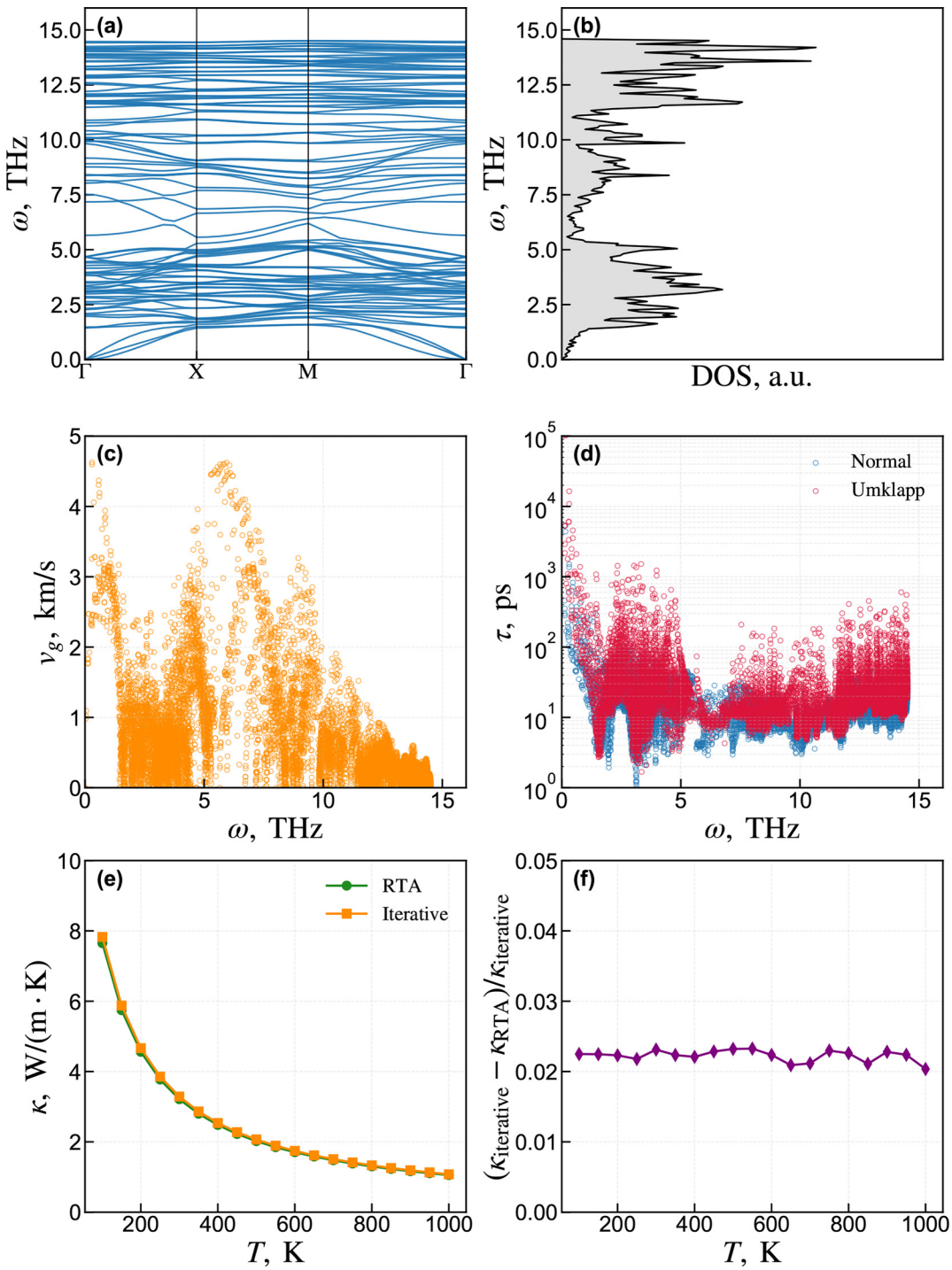

FIG. 5. Phonon transport properties of the 1 nm silicon thin film with 2 × 2 surface reconstruction: (a) Phonon dispersion relations along Γ-X-M-Γ, exhibiting zone folding and flexural modes; (b) density of states (DOS) showing confinement-induced peaks; (c) phonon group velocities, showing significant suppression compared to bulk; and (d) relaxation times (τ) decomposed into normal (blue) and Umklapp (red) processes, revealing the dominance of anharmonic scattering in the thin film regime; (e) temperature dependence of the lattice thermal conductivity (κ) calculated using the Relaxation Time Approximation (RTA) and iterative methods; and (f) the relative deviation of the RTA thermal conductivity from the iterative solution, $(\kappa_p^{\text{iter}} - \kappa_p^{\text{RTA}})/\kappa_p^{\text{iter}}$, as a function of temperature.

sampling feasible (requiring approximately 20.0 and 80.0 h, respectively), the CS-NEP workflow drastically reduces the required configurations to just 500 for both thicknesses. Consequently, the extraction time drops to 4.0 h for the 1 nm film and 10.0 h for the 2 nm film, representing a 5× and 8× acceleration relative to the NEP (FDM) benchmark, respectively.

Crucially, the core advantage of the CS-NEP approach is its favorable scaling behavior for low-symmetry systems. Unlike standard FDM, which scale steeply when crystalline symmetries are broken, CS approach uses stochastic sampling. Its computational cost depends on the sparsity of the solution rather than explicit symmetry constraints. This is clearly validated by our 1 and 2 nm film results: while FDM requires over ten times more structures (from ∼ 12 k to ∼ 162 k) for the larger system, the CS approach consistently needs only 500 structures. Consequently, the efficiency gap between CS and FDM widens significantly as the system grows. This allows the CS-NEP workflow to effectively overcome the scaling bottleneck of traditional methods for large structures with complex surfaces or interfaces.

In terms of applicability, conventional FDM remains highly efficient for high-symmetry bulk crystals where the number of independent force constants is minimal. However, its computational cost becomes prohibitive as symmetry is broken. Conversely, the CS-based approach is uniquely suited for complex, low-symmetry systems such as interfaces, defects, or reconstructed surfaces, where sparsity is maintained by the locality of atomic interactions.

Having established the computational efficiency, we proceed to validate the accuracy of the framework by benchmarking the lattice dynamical properties and foundational interatomic force constants (IFCs) of bulk silicon against DFT calculations. Figure 4 compares the phonon dispersion relations, density of states (DOS), second- and third-order IFCs, group velocities (v_g), and relaxation times (τ) at 300 K.

Regarding harmonic properties [Figs. 4(a)–4(c)], the NEP-derived dispersion curves (solid blue lines) exhibit excellent agreement with DFT benchmarks (red dashed lines) throughout the Brillouin zone [Fig. 4(a)]. The precise matching of acoustic branches near Γ confirms the accurate reproduction of elastic constants and sound velocities. Similarly, the flattening of optical branches and the corresponding van Hove singularities in the DOS [Fig. 4(b)] are captured with high fidelity. This macroscopic agreement is fundamentally underpinned by the tensor-level accuracy of the second-order IFCs (Φ_{ij}). As shown in the parity plot [Fig. 4(c)], the NEP predictions align with the explicit DFT values across all interaction ranges, yielding a high coefficient of determination ($R^2 = 0.997$).

Crucial for transport predictions, the group velocity distribution [Fig. 4(e)] is well reproduced across the spectrum, particularly for the high-velocity acoustic modes that dominate heat conduction. Furthermore, the relaxation times [Fig. 4(f)]—which encode third-order anharmonicity—show consistent frequency scaling between NEP and DFT. While the excellent agreement in relaxation times is highly encouraging, such macroscopic consistency could theoretically arise from a fortuitous cancelation of errors within the massive anharmonic matrix elements. To definitively rule out this possibility, we present a direct, quantitative comparison of the third-order IFC tensors (Φ_{ijk}) in Fig. 4(d). The symmetrical logarithmic plot explicitly maps the magnitude distribution across over four orders of magnitude. The CS-NEP workflow successfully captures the both the strong nearest-neighbor and long-range interactions with a very low relative root mean square error (RRMSE = 0.123) and high coefficient of determination ($R^2 = 0.9895$). This tensor-level validation confirms that the CS-based workflow genuinely recovers the true physical anharmonic interactions, ensuring absolute reliability for subsequent thermal transport calculations.

We next analyze the confinement-induced transport phenomena in the 1 nm silicon thin film, with results summarized in Fig. 5. The dispersion relations along the high-symmetry path Γ−X−M−Γ [Fig. 5(a)] differ drastically from the bulk behavior. Finite thickness along the z-direction induces severe phonon zone folding, generating a dense manifold of sub-bands and flattening the optical branches. A hallmark of this quasi-two-dimensional system is the quadratic dispersion of the flexural acoustic (ZA) modes near the Γ point.[36] Consequently, the phonon DOS [Fig. 5(b)] exhibits a high density of van Hove singularities, in sharp contrast to the continuous spectrum of bulk silicon.

These structural constraints significantly alter the microscopic transport descriptors. The phonon group velocities [Fig. 5(c)] are markedly suppressed, with a maximum value of approximately 4.5 km/s—nearly half that of the bulk (∼8.5 km/s). This reduction stems directly from the diminished band curvature ($\partial\omega/\partial k$) induced by zone folding and the localization of vibrational modes at the reconstructed surfaces.[5]

The impact of nanostructuring is equally pronounced in the phonon relaxation times, as shown in Fig. 5(d). Our workflow enables the explicit decomposition of scattering rates into normal (N) and Umklapp (U) processes. This separation is essential for distinguishing momentum-conserving interactions from resistive ones, thereby providing the necessary resolution to investigate potential phonon hydrodynamic[37,51] effects in such nanostructures.

Figure 5(e) shows the BTE-based lattice thermal conductivity (κ_p) of a 1 nm silicon thin film as a function of temperature. The results of RTA (blue) and the iterative method (red) show excellent consistency across the entire temperature range of 100–1000 K. To quantify this difference, Fig. 5(f) shows the relative deviation, calculated as $(\kappa_p^{\text{iter}} - \kappa_p^{\text{RTA}})/\kappa_p^{\text{iter}}$. The maximum deviation is less than 3% near room temperature. This small difference is consistent with the transport physics of silicon.

We apply the Wigner transport formalism to resolve the macroscopic lattice thermal conductivity (κ) into contributions arising from the dual particle-wave nature of phonons. Figure 6 presents this decomposition into the particle-like population channel (κ_p) and the wave-like coherence channel (κ_c).

Figures 6(a) and 6(c) display the temperature dependence of thermal conductivity for the 1 nm film with varying length. The population term κ_p [Fig. 6(a)] exhibits a monotonic increase with channel length L, signifying the crossover from the ballistic regime—limited by contact boundary scattering—to the diffusive regime dominated by intrinsic scattering. The finite length L is introduced through a boundary-scattering correction to the phonon relaxation time via Matthiessen's rule, where $\tau_{\text{tot},\lambda}^{-1} = \tau_{\text{ph-ph},\lambda}^{-1} + |v_\lambda|/L$. This ballistic signature is most prominent at low temperatures in short channels, where the intrinsic phonon mean free path exceeds the system dimensions. In contrast, at temperatures above 800 K, the convergence of curves for varying lengths indicates that intrinsic Umklapp scattering (scaling as T^{-1}) becomes the rate-limiting mechanism.

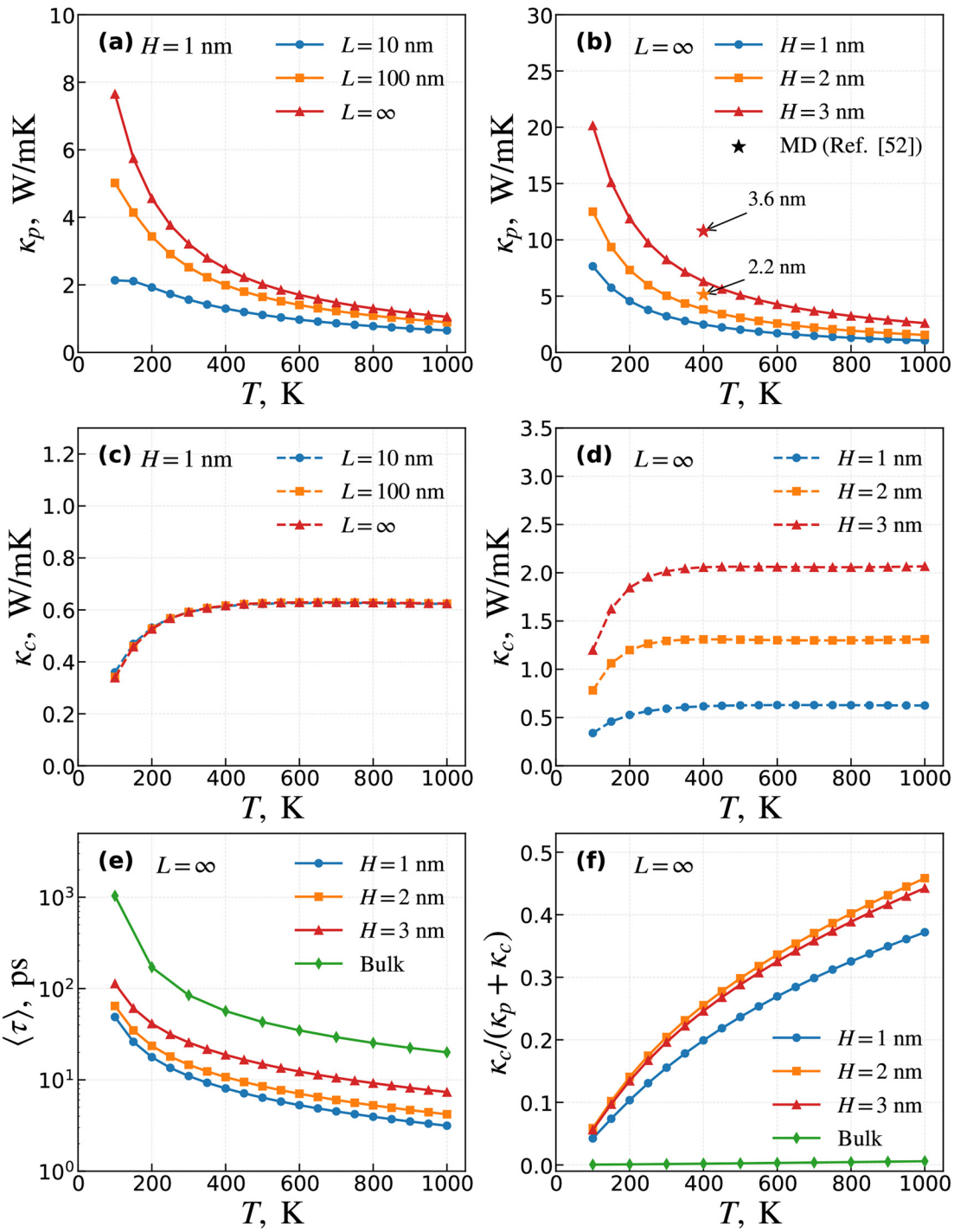

FIG. 6. Temperature dependence of the resolved lattice thermal conductivity components calculated via the Wigner transport equation. (a) and (c) Evolution of the (a) particle-like population term κ_p and (c) wave-like coherence term κ_c with varying lengths L for a fixed 1 nm film. (b) and (d) Impact of geometric confinement on (b) κ_p and (d) κ_c for varying film thicknesses ($H = 1, 2, 3$ nm) in the diffusive limit ($L \to \infty$). In (b), MD data for 2.2 and 3.6 nm films at 400 K are taken from Ref. 52 for comparison. (e) Comparison of the heat-capacity-weighted average relaxation time $\langle\tau\rangle$ for bulk silicon and films with different thicknesses. (f) Temperature dependence of the relative contribution of the coherence term to the total thermal conductivity, $\kappa_c/(\kappa_p + \kappa_c)$, for bulk silicon and films with different thicknesses.

The impact of geometric confinement (thickness $H = 1, 2, 3$ nm) in the diffusive limit ($L \to \infty$) is detailed in Figs. 6(b) and 6(d). For thinner films, the population component κ_p [Fig. 6(b)] is markedly suppressed. This reduction originates from the truncation of long-wavelength modes and the intensified boundary-scattering-induced by surface reconstruction. The validity of our framework is further corroborated by the excellent agreement between our results and molecular dynamics (MD) data for 2.2 and 3.6 nm films at 400 K,[52] which captures the full anharmonicity of the system. Theoretically, κ_p is expected to asymptotically recover toward the bulk limit as thickness increases. While capturing this convergence requires simulating significantly larger supercells, the scalability of our CS-NEP workflow establishes a solid foundation for such large-scale characterizations in future work.

Significantly, the coherence channel κ_c makes a substantial contribution to the total conductivity, as evidenced in Figs. 6(c) and 6(d). Distinct from the particle-like propagation of κ_p, κ_c originates from quantum interference between eigenstates. This inter-band tunneling mechanism is amplified in these nanofilms by extensive band folding, which maximizes the off diagonal elements of the velocity operator. Crucially, within the investigated 1–3 nm range, κ_c exhibits a monotonic increase. This trend indicates that transport physics in this ultra-thin regime is governed by spectral crowding, where the proliferation of phonon sub-bands as thickness increases yields a significantly denser spectrum with diminished inter-branch energy spacings. Consequently, this spectral densification directly promotes inter-band tunneling probabilities.

It is essential to distinguish the 2×2 surface reconstruction used here from conventional rough boundary scattering. While the latter relies on random disorder to induce momentum-randomizing diffuse reflection, the 2×2 reconstruction preserves in-plane translational symmetry. Consequently, the observed transport modifications stem from deterministic symmetry breaking and phonon zone folding. Thus, the suppression of κ_p and the evolution of κ_c should be interpreted as intrinsic band-structure effects rather than extrinsic, roughness-induced scattering.

To further elucidate the impact of geometric confinement on phonon scattering, the heat-capacity-weighted average relaxation time, $\langle \tau \rangle = \sum_\lambda C_\lambda \tau_\lambda / \sum_\lambda C_\lambda$, is calculated for bulk silicon and nanofilms, as presented in Fig. 6(e). We observe that τ decreases by approximately one order of magnitude relative to the bulk. This reduction is driven by two concurrent mechanisms: (1) the increased scattering phase space associated with subband formation in the nanostructure and (2) the enhanced anharmonic scattering rates driven by the 2×2 surface reconstruction, which introduces stronger phonon-phonon interactions compared to the bulk.

Furthermore, Fig. 6(f) quantifies the relative importance of the coherence channel by plotting the ratio $\kappa_c/(\kappa_p + \kappa_c)$ as a function of temperature. As temperature increases, the relative contribution of wave-like transport rises significantly across all investigated thicknesses. This behavior stems from the different temperature dependencies of the two channels: while κ_p is sharply suppressed by the T^{-1} scaling of Umklapp scattering, the coherence term κ_c is less sensitive to these scattering processes and can even be enhanced by the broadening of phonon linewidths, which facilitates inter-band tunneling. Notably, the relative contribution of the coherence term, $\kappa_c/(\kappa_p + \kappa_c)$, follows a non-monotonic trend with thickness, peaking at 2 nm. This shift reflects a competition between spectral crowding and bulk-like recovery: while increasing thickness from 1 to 2 nm reduces energy spacings via band folding to boost inter-band tunneling (κ_c), further growth to 3 nm allows the particle-like κ_p to recover more rapidly as boundary suppression diminishes, thereby slightly reducing the coherence channel's relative percentage.

IV. CONCLUSION

In summary, we have developed and validated an integrated computational paradigm that synergizes the high-throughput sampling of NEP with the data-efficient extraction of CS. This framework successfully overcomes the prohibitive $O(N^3)$ scaling of traditional finite-displacement methods, enabling the determination of high-order interatomic force constants for complex nanostructures with *ab initio* accuracy but at a fraction of the computational cost.

By applying this workflow to silicon nanofilms with 2×2 surface reconstructions, we have decoupled the competing microscopic mechanisms governing thermal transport in the sub-5 nm regime. Our findings demonstrate that while geometric confinement significantly suppresses the particle-like population contribution (κ_p), driven by band-folding-induced phase space expansion and surface-enhanced anharmonicity, the wave-like coherence contribution (κ_c) becomes increasingly prominent due to spectral crowding. The rigorous application of the WTE reveals that neglecting these coherence effects leads to a fundamental underestimation of thermal conductivity in ultra-thin regimes.

This methodology provides a robust, scalable, and automated route for the high-throughput thermal characterization of low-dimensional materials, especially those with broken symmetries such as interfaces, defects, and reconstructed surfaces. The established CS-NEP workflow bridges the gap between fundamental phonon physics and engineering-scale thermal design, offering critical insights into the development of next-generation, thermally-optimized nanoelectronic devices.

ACKNOWLEDGMENTS

F. Yin, S. Liu, and Y. Dong gratefully acknowledge financial support from the China Scholarship Council (No. 202408090635 for F. Yin, No. 202308090243 for S. Liu, and No. 202406290035 for Y. Dong). K. Xu acknowledges support from the Bohai University On-campus Doctoral Start-up Project Funding.

AUTHOR DECLARATIONS

Conflict of Interest

The authors have no conflicts to disclose.

Author Contributions

Fei Yin: Data curation (equal); Formal analysis (equal); Investigation (equal); Validation (equal); Writing – original draft (equal). **Shixian Liu:** Conceptualization (equal); Investigation (equal); Methodology (equal); Writing – original draft (equal). **Yiming Dong:** Formal analysis (supporting); Validation

(supporting); Writing – review & editing (supporting). **A. A. Barinov:** Methodology (equal); Supervision (equal); Writing – original draft (equal). **Ke Xu:** Formal analysis (equal); Investigation (equal); Methodology (equal); Writing – original draft (equal). **V. I. Khvesyuk:** Conceptualization (equal); Supervision (equal); Writing – review & editing (equal).

DATA AVAILABILITY

The data and scripts supporting the findings of this study are available in GitHub at https://github.com/lyushisyan/NEP-kappa, Ref. 53. The data that support the findings of this study are available from the corresponding author upon reasonable request.

APPENDIX A: NEP TRAINING HYPERPARAMETERS

This appendix details the specific hyperparameters employed for training the NEP-SiNWs model (version 4) using the SNES optimization algorithm. Table II lists the settings for the descriptor construction and the neural network architecture.

The choice of hyperparameters in Table II is based on the covalent nature of silicon and the architectural efficiency of the NEP model.[30] For covalent systems like silicon, we utilize radial and angular basis sizes ($n_{\max} = 10$) to provide a balanced description of the atomic environment. The angular expansion order $l_{\max} = 4$ is selected to accurately resolve the directional bonding of the diamond lattice. Notably, we employ a single hidden layer with 60 neurons; while deep potential models often require multi-layer architectures to compensate for simpler descriptors, the sophisticated atom-environment descriptors in NEP allow this shallow network to achieve high accuracy with superior computational efficiency, as confirmed by our convergence tests.

APPENDIX B: CONVERGENCE ANALYSIS

To ensure the reliability of the WTE-based thermal conductivity calculations, we performed systematic convergence tests on both the number of atomic configurations N_{struc} for CS-based IFC extraction and the reciprocal q-mesh density. As shown in Fig. 7, the lattice thermal conductivity components (κ_p and κ_c) exhibit excellent stability when the number of sampled structures N_{struc} exceeds 400 and the q-mesh reaches $21 \times 21 \times 1$.

TABLE II. Hyperparameters for the NEP-SiNWs training (version 4). The model utilizes a single hidden layer with 60 neurons and separates radial and angular descriptors.

Parameter	Value	Description
Version	4	NEP generation (NEP4)
Type	1 (Si)	Elemental type
Cutoff	5.5 5.5	Radial and angular cutoffs (Å)
n_max	10 10	Radial and angular basis size
basis_size	12 12	Number of basis functions
l_max	4 2	Angular expansion order
Neuron	60	Hidden layer neurons
λ_e	1.0	Energy loss weight
λ_f	1.0	Force loss weight
λ_v	0.1	Virial loss weight
Batch	1000	Training batch size
Generation	5×10^5	SNES generations

APPENDIX C: INPUT CONFIGURATION EXAMPLES

The automated workflow is driven by a unified input interface. The following listings illustrate the configuration scripts used for the standard benchmark (FDM) and the accelerated workflow (CS), respectively. These parameters correspond to the simulation settings discussed in the main text.

```
# --- System & Potential ---
--poscar       Structure/POSCAR
--nep_model    NEP/Si_2025_XuKe.txt
--do_relax     false

# --- Supercell Definitions ---
--dim          4 4 1

# --- Workflow Control ---
--fc2fc3       true
--method       rta
--use_hiphive false     # Standard FD mode
--wigner       true

# --- Calculation Parameters ---
--mesh         21 21 1
--temps        100 1000 50
```

Listing 1: Input configuration for the standard FDM.

```
# --- System & Potential ---
--poscar       Structure/POSCAR
--nep_model    NEP/Si_2025_XuKe.txt
--do_relax     false

# --- Supercell Definitions ---
--dim          4 4 1

# --- HiPhive Specifics (Accelerated) ---
--use_hiphive  true      # Activates CS solver
--n_structures 500       # Number of structures
--rattle_std   0.03      # Displacement std
--min_dist     2.2       # Min atomic distance
--cutoffs      5.0 4.0   # For 2nd and 3rd order
    FCs

# --- Workflow Control ---
--fc2fc3       true
--method       rta
--wigner       true

# --- Calculation Parameters ---
--mesh         21 21 1
--temps        100 1000 50
```

Listing 2: Input configuration for the accelerated CS method.

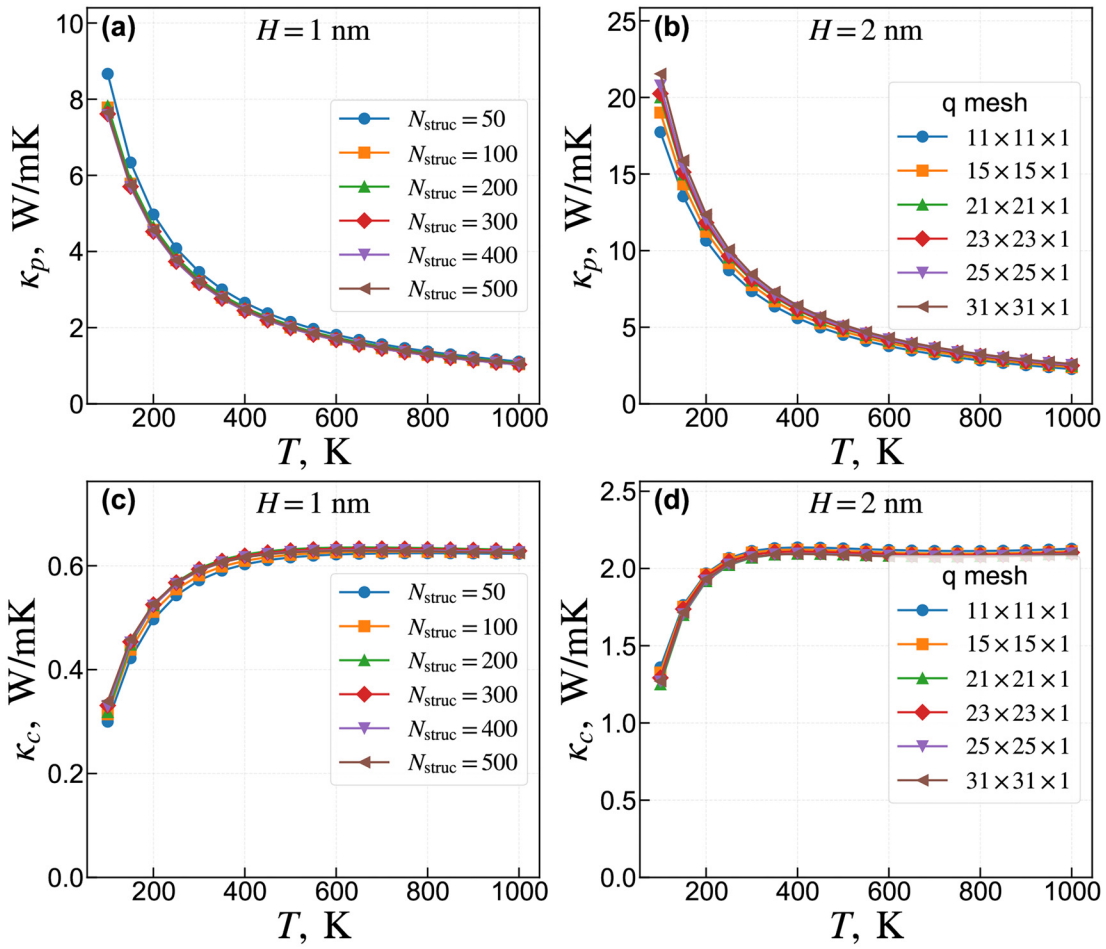

FIG. 7. Convergence tests of the resolved lattice thermal conductivity components for silicon films. (a) and (c) Evolution of (a) the population term κ_p and (c) the coherence term κ_c with respect to the number of sampled structures N_{struc} for $H = 1$ nm. (b) and (d) Dependence of (b) κ_p and (d) κ_c on the q-mesh density ($N \times N \times 1$) for $H = 2$ nm.

The CS-based IFC extraction parameters are chosen based on physical constraints and established benchmarks for silicon.[40,41] A displacement amplitude of $\sigma = 0.03$ Å is employed to balance the force signal-to-noise ratio with the validity of the third-order Taylor expansion; as shown in Fig. 7, the convergence of the extracted properties is primarily determined by the number of configurations N_{struc}. For the cutoff radii, 5.0 Å is used for second-order IFCs to encompass the third-nearest neighbor shell and ensure accurate group velocities, while 4.0 Å is selected for third-order IFCs to capture the dominant short-range three-phonon scattering processes while maintaining the stability of the compressed sensing solver.[41]

REFERENCES

[1]M. M. Waldrop, "The chips are down for Moore's law," Nature **530**, 144–147 (2016).
[2]A. L. Moore and L. Shi, "Emerging challenges and materials for thermal management of electronics," Mater. Today **17**, 163–174 (2014).
[3]P. Chantrenne, J. L. Barrat, X. Blase, and J. D. Gale, "An analytical model for the thermal conductivity of silicon nanostructures," J. Appl. Phys. **97**, 104318 (2005).
[4]Y. Ma, "Size-dependent thermal conductivity in nanosystems based on non-Fourier heat transfer," Appl. Phys. Lett. **101**, 211905 (2012).
[5]S. Liu, Z. Zong, F. Yin, V. Khvesyuk, and N. Yang, "Quantifying particle and wave effects in phonon transport of pillared graphene nanoribbons," Int. J. Therm. Sci. **217**, 110067 (2025).
[6]F. Yin, S. Liu, A. A. Barinov, and V. I. Khvesyuk, "An enhanced framework for wave reflection from a periodically rough boundary," Phys. B: Condens. Matter **716**, 417743 (2025).
[7]Z. Zhou, Y. He, S. Liu, L. Yang, and N. Yang, "Effect of non-Fourier heat transport on temperature distribution in high bandwidth memory," IEEE Trans. Electron Devices **73**, 561–568 (2026).
[8]I. Ponomareva, D. Srivastava, and M. Menon, "Thermal conductivity in thin silicon nanowires: Phonon confinement effect," Nano Lett. **7**, 1155–1159 (2007).

[9]M.-J. Huang, T.-M. Chang, W.-Y. Chong, C.-K. Liu, and C.-K. Yu, "A new lattice thermal conductivity model of a thin-film semiconductor," Int. J. Heat Mass Transfer **50**, 67–74 (2007).
[10]Y. Yu, C. Yang, M. Baggioli, A. E. Phillips, A. Zaccone, L. Zhang, R. Kajimoto, M. Nakamura, D. Yu, and L. Hong, "The $\omega 3$ scaling of the vibrational density of states in quasi-2D nanoconfined solids," Nat. Commun. **13**, 3649 (2022).
[11]S.-X. Liu, A. A. Barinov, F. Yin, and V. I. Khvesyuk, "Determination of thermal properties of unsmooth Si-nanowires," Chin. Phys. Lett. **41**, 016301 (2024).
[12]A. Zaccone, "Phonon-confinement theory of thermal conductivity in ultrathin silicon films," J. Appl. Phys. **138**, 225305 (2025).
[13]W. Li, J. Carrete, N. A. Katcho, and N. Mingo, "ShengBTE: A solver of the Boltzmann transport equation for phonons," Comput. Phys. Commun. **185**, 1747–1758 (2014).
[14]H. Bao, J. Chen, X. Gu, and B. Cao, "A review of simulation methods in micro/nanoscale heat conduction," ES Energy Environ. **1**, 16–55 (2018).
[15]A. Togo, "First-principles phonon calculations with phonopy and phono3py," J. Phys. Soc. Jpn. **92**, 012001 (2023).
[16]Z. Han, X. Yang, W. Li, T. Feng, and X. Ruan, "FourPhonon: An extension module to ShengBTE for computing four-phonon scattering rates and thermal conductivity," Comput. Phys. Commun. **270**, 108179 (2022).
[17]A. J. H. McGaughey, A. Jain, H.-Y. Kim, and B. Fu, "Phonon properties and thermal conductivity from first principles, lattice dynamics, and the Boltzmann transport equation," J. Appl. Phys. **125**, 011101 (2019).
[18]A. J. H. McGaughey, L. Lindsay, H. Bao, T. Hamakawa, R. Juneja, S. Li, W. Li, R. Masuki, F. Meng, H. Meng, T. Pandey, C. Shao, J. Shiomi, T. Tadano, A. Togo, A. Wang, and X. Zhang, "Phonon olympics: Phonon property and lattice thermal conductivity benchmarking from open-source packages," J. Appl. Phys. **138**, 135108 (2025).
[19]T. Feng and X. Ruan, "Prediction of spectral phonon mean free path and thermal conductivity with applications to thermoelectrics and thermal management: A review," J. Nanomater. **2014**, 206370 (2014).
[20]J. Behler and M. Parrinello, "Generalized neural-network representation of high-dimensional potential-energy surfaces," Phys. Rev. Lett. **98**, 146401 (2007).
[21]J. Behler, "Perspective: Machine learning potentials for atomistic simulations," J. Chem. Phys. **145**, 170901 (2016).
[22]A. P. Bartók, M. C. Payne, R. Kondor, and G. Csányi, "Gaussian approximation potentials: The accuracy of quantum mechanics, without the electrons," Phys. Rev. Lett. **104**, 136403 (2010).
[23]A. P. Bartók, J. Kermode, N. Bernstein, and G. Csányi, "Machine learning a general-purpose interatomic potential for silicon," Phys. Rev. X **8**, 041048 (2018).
[24]B. Mortazavi, E. V. Podryabinkin, I. S. Novikov, S. Roche, T. Rabczuk, X. Zhuang, and A. V. Shapeev, "Efficient machine-learning based interatomic potentialsfor exploring thermal conductivity in two-dimensional materials," J. Phys.: Mater. **3**, 02LT02 (2020).
[25]B. Mortazavi, E. V. Podryabinkin, I. S. Novikov, T. Rabczuk, X. Zhuang, and A. V. Shapeev, "Accelerating first-principles estimation of thermal conductivity by machine-learning interatomic potentials: A MTP/ShengBTE solution," Comput. Phys. Commun. **258**, 107583 (2021).
[26]L. Guo, Y. Liu, L. Yang, and B. Cao, "Lattice dynamics modeling of thermal transport in solids using machine-learned atomic cluster expansion potentials: A tutorial," J. Appl. Phys. **137**, 081101 (2025).
[27]X. Qian and R. Yang, "Machine learning for predicting thermal transport properties of solids," Mater. Sci. Eng.: R: Rep. **146**, 100642 (2021).
[28]Y. Qin, Z. Zong, J. Che, T. Li, H. Fang, and N. Yang, "A significant enhancement in thermal conductivity of plastic crystals under compressive strain by deep potential molecular dynamics," Appl. Phys. Lett. **126**, 104101 (2025).
[29]Z. Zong, Y. Qin, J. Zhan, H. Fang, and N. Yang, "Machine learning potential for predicting thermal conductivity of θ-phase and amorphous tantalum nitride," Int. J. Heat Mass Transfer **257**, 128155 (2026).
[30]Z. Fan, Z. Zeng, C. Zhang, Y. Wang, K. Song, H. Dong, Y. Chen, and T. Ala-Nissila, "Neuroevolution machine learning potentials: Combining high accuracy and low cost in atomistic simulations and application to heat transport," Phys. Rev. B **104**, 104309 (2021).
[31]Z. Fan, Y. Wang, P. Ying, K. Song, J. Wang, Y. Wang, Z. Zeng, K. Xu, E. Lindgren, J. M. Rahm, A. J. Gabourie, J. Liu, H. Dong, J. Wu, Y. Chen, Z. Zhong, J. Sun, P. Erhart, Y. Su, and T. Ala-Nissila, "GPUMD: A package for constructing accurate machine-learned potentials and performing highly efficient atomistic simulations," J. Chem. Phys. **157**, 114801 (2022).
[32]Z. Fan, "Improving the accuracy of the neuroevolution machine learning potential for multi-component systems," J. Phys.: Condens. Matter **34**, 125902 (2022).
[33]K. Song, R. Zhao, J. Liu, Y. Wang, E. Lindgren, Y. Wang, S. Chen, K. Xu, T. Liang, P. Ying *et al.*, "General-purpose machine-learned potential for 16 elemental metals and their alloys," Nat. Commun. **15**, 10208 (2024).
[34]T. Liang, K. Xu, E. Lindgren, Z. Chen, R. Zhao, J. Liu, E. Berger, B. Tang, B. Zhang, Y. Wang, K. Song, P. Ying, N. Xu, H. Dong, S. Chen, P. Erhart, Z. Fan, T. Ala-Nissila, and J. Xu, "Nep89: Universal neuroevolution potential for inorganic and organic materials across 89 elements" (2025), arXiv:2504.21286 [cond-mat.mtrl-sci].
[35]Z. Tang, X. Wang, J. Li, C. He, M. Chen, C. Tang, and T. Ouyang, "Weak $s-d$ orbital bonding induces strong phonon anharmonicity and unconventional mass-dependent behavior of lattice thermal conductivity in $CaTiF_6$," Phys. Rev. Mater. **9**, 093401 (2025).
[36]S. Liu, G. Zhang, F. Yin, A. A. Barinov, V. I. Khvesyuk, and N. Yang, "Temperature dependence of specific heat capacity of nanostructures via neuroevolution machine-learned potential," J. Appl. Phys. **138**, 104301 (2025).
[37]K. Xu, Y. Li, D. Ding, T. Liang, J. Wu, and J. Xu, "Critical size transitions in silicon nanowires: Amorphization, phonon hydrodynamics, and thermal conductivity," J. Phys. Chem. Lett. **16**, 8580–8587 (2025).
[38]X. Wu, Z. Wu, T. Liang, Z. Fan, J. Xu, M. Nomura, and P. Ying, "Phonon coherence and minimum thermal conductivity in disordered superlattices," Phys. Rev. B **111**, 085413 (2025).
[39]T. Liang, K. Xu, P. Ying, W. Jiang, M. Han, X. Wu, W. Ouyang, Y. Yao, X. Zeng, Z. Ye, Z. Fan, and J. Xu, "Probing the ideal limit of interfacial thermal conductance in two-dimensional van der Waals heterostructures," npj Comput. Mater. **12**, 11 (2026).
[40]F. Eriksson, E. Fransson, and P. Erhart, "The hiphive package for the extraction of high-order force constants by machine learning," Adv. Theory Simul. **2**, 1800184 (2019).
[41]E. Fransson, F. Eriksson, and P. Erhart, "Efficient construction of linear models in materials modeling and applications to force constant expansions," npj Comput. Mater. **6**, 135 (2020).
[42]Y. Song, S. Li, P. Lin, J. Li, T. Ouyang, C. Tang, and C. He, "First-principles predictions of the diversity in the atomic structures and electronic properties of the reconstructed Si(111)-7 × 7 surface," Phys. Chem. Chem. Phys. **28**, 5554–5560 (2026).
[43]M. Simoncelli, N. Marzari, and F. Mauri, "Unified theory of thermal transport in crystals and glasses," Nat. Phys. **15**, 809–813 (2019).
[44]M. Simoncelli, N. Marzari, and F. Mauri, "Wigner formulation of thermal transport in solids," Phys. Rev. X **12**, 041011 (2022).
[45]J. A. Appelbaum, G. A. Baraff, and D. R. Hamann, "The Si(100) surface. III. Surface reconstruction," Phys. Rev. B **14**, 588–601 (1976).
[46]A. Ramstad, G. Brocks, and P. J. Kelly, "Theoretical study of the Si(100) surface reconstruction," Phys. Rev. B **51**, 14504–14523 (1995).
[47]K. Xu, H. Bu, S. Pan, E. Lindgren, Y. Wu, Y. Wang, J. Liu, K. Song, B. Xu, Y. Li, T. Hainer, L. Svensson, J. Wiktor, R. Zhao, H. Huang, C. Qian, S. Zhang, Z. Zeng, B. Zhang, B. Tang, Y. Xiao, Z. Yan, J. Shi, Z. Liang, J. Wang, T. Liang, S. Cao, Y. Wang, P. Ying, N. Xu, C. Chen, Y. Zhang, Z. Chen, X. Wu, W. Jiang, E. Berger, Y. Li, S. Chen, A. J. Gabourie, H. Dong, S. Xiong, N. Wei, Y. Chen, J. Xu, F. Ding, Z. Sun, T. Ala-Nissila, A. Harju, J. Zheng, P. Guan, P. Erhart, J. Sun, W. Ouyang, Y. Su, and Z. Fan, "GPUMD 4.0: A high-performance molecular dynamics package for versatile materials simulations with machine-learned potentials," Mater. Genome Eng. Adv. **3**, e70028 (2025).
[48]T. Schaul, T. Glasmachers, and J. Schmidhuber, "High dimensions and heavy tails for natural evolution strategies," in *Proceedings of the 13th Annual*

Conference on Genetic and Evolutionary Computation (ACM, Dublin, 2011), pp. 845–852.
[49]Y. Zhang and X. Xu, "Machine learning the magnetocaloric effect in manganites from compositions and structural parameters," AIP Adv. **10**, 035220 (2020).
[50]B. Jin and X. Xu, "Machine learning natural gas price predictions," Energy Sci. **01**, 2550001 (2025).
[51]G. Chen, "Non-Fourier phonon heat conduction at the microscale and nanoscale," Nat. Rev. Phys. **3**, 555–569 (2021).
[52]C. J. Gomes, M. Madrid, J. V. Goicochea, and C. H. Amon, "In-plane and out-of-plane thermal conductivity of silicon thin films predicted by molecular dynamics," J. Heat Transfer **128**, 1114–1121 (2006).
[53]S. Liu and F. Yin (2026). "NEP-kappa," GitHub. https://github.com/lyushisyan/NEP-kappa (last accessed 10 Jan 10, 2026).